RSC Advances

PAPER

View Article Online
View Journal | View Issue

Cite this: *RSC Adv.*, 2014, **4**, 57054

Porous (001)-faceted Zn-doped anatase TiO_2 nanowalls and their heterogeneous photocatalytic characterization†

Siti Khatijah Md Saad,[a] Akrajas Ali Umar,*[a] Hong Quan Nguyen,[b] Chang Fu Dee,[a] Muhamad Mat Salleh[a] and Munetaka Oyama[c]

Received 21st August 2014
Accepted 17th October 2014

DOI: 10.1039/c4ra08991j

www.rsc.org/advances

The synthesis of a poriferous and high energy (001) faceted anatase Zn-doped TiO_2 nanowall (ZnTNW), vertically grown on an indium tin oxide substrate, is presented. The ZnTNW was prepared using a modified liquid phase deposition method using zinc nitrate ($Zn(NO_3)_2 \cdot xH_2O$) as a fluoride scavenger in the presence of hexamethylenetetramine. In a typical procedure, the ZnTNW nanowall with length and thickness of approximately 2 μm and 60 nm, respectively, can be obtained from the reaction during a 5 h growth process. X-ray diffraction analysis shows that the nanowall has an anatase structure with a dominant high energy (001) basal plane. Meanwhile, the X-ray energy dispersive analysis confirms the presence of Zn in the TiO_2 nanowall. High resolution transmission electron microscopy analysis results reveal, surprisingly, that the ZnTNW is single crystalline in nature although it has a highly porous (surface and bulk) structure. Photocatalytic properties of the ZnTNW were examined in the degradation of methylene blue. It was found that the ZnTNW exhibits excellent photocatalytic efficiency with kinetic reaction rate, turnover number and turnover frequency as high as 0.004 min^{-1}, 760 and 11 min^{-1}, respectively. The photocatalytic performance of the ZnTW was found to be higher for about 10% and 50% than the pristine TiO_2 nanowalls and (001) faceted poriferous TiO_2 microtablet, which reflected the effective effect of the Zn doping. The ZnTNW may find potentially use in photocatalytic heterogeneous applications.

Introduction

The synthesis of an anatase polymorph of titanium dioxide (TiO_2) characterized with a wide area (001) facet has recently become the focus of attention for enhanced performance in applications that range from photocatalysis to optoelectronic device fabrication and solar cell applications. Its structural, electronic and optical properties have been well reviewed in recent publications.[1,2] With the surface containing abundant unsaturated Ti atoms, strained Ti–O–Ti bonds on its outer surface and relaxed surface energy as high as 1.44 Jm^{-2} make the (001) faceted anatase TiO_2 chemically active for a wide range of physico-chemical reactions.[3–6] For example, the water molecule is readily split on the surface of (001) and efficient interfacial charge transfer was observed in the dye sensitized solar cell utilizing anatase TiO_2 that is rich with this plane. Unfortunately, contrary to its intriguing properties, the synthesis of anatase TiO_2 with (001) plane is challenging and limited because of its nature to easily transform into the (101) face, the most stable and less reactive face, as the result of high surface energy. Therefore, the chemical synthetic method that enables the preparation of anatase TiO_2 nanostructures that are bounded by (001) facets is required and the effort toward this objective should be continuously demonstrated.

So far, several methods are available for the preparation of an anatase TiO_2 nanostructure with a shape containing large area (001) facet. An excellent approach to this was developed by Lu and co-workers. By using titanium tetrafluoride as the precursor materials and hydrofluoric acid as the morphology control agent, they successfully realized the formation of a large percentage of (001) facet anatase TiO_2.[7–9] Quite recently, Wang and co-workers demonstrated a new method to synthesise single crystal anatase TiO_2 with a dominant (001) facet *via* a simple hydrothermal decomposition of TiO_2 powder using peroxide. Although high quality (001) faceted anatase TiO_2 can be produced using these methods, the structure is an atomically smooth surface, rendering a low surface area as well as "less-reactivity" as the catalytic and surface reaction favors the occurrence of the defect or kink sites.[10] In addition, these

[a]*Institute of Microengineering and Nanoelectronics, Universiti Kebangsaan Malaysia, 43600 UKM Bangi, Selangor, Malaysia. E-mail: akrajas@ukm.edu.my*

[b]*Dept. Materials Science and Engineering, National Chiao Tung University, Hsin Chu, Taiwan, Republic of China*

[c]*Department of Material Chemistry, Graduate School of Engineering, Kyoto University, Nishikyo-ku, Kyoto, 615-8520, Japan*

† Electronic supplementary information (ESI) available: FESEM images of Zn doped TiO_2 prepared under different temperature, HMT and growth time and PTM. See DOI: 10.1039/c4ra08991j

methods realize the formation of (001) faceted anatase TiO_2 in the solution that may limit their usage in particular applications, such as solar cells, optoelectronic devices and heterogeneous catalysis. Therefore, the growth of (001) faceted anatase TiO_2 nanostructure directly on the substrate surface is of considerable importance.[11]

Although pristine anatase TiO_2 has shown excellent performance in existing applications, metal doping has been discovered to further improve its performance. Transition metals doping, for example, particularly with Zn, enhanced the electronic and catalytic properties of TiO_2[12] up to multiple orders higher, which was the result of the Fermi level increasing, the reduction of conduction band minimum and the formation of impurity energy level or the increase in the surface oxygen vacancies upon doping.[13–15] This resulted in the shifting of the energy band gap to the visible region, sensitizing its physicochemical reactivity.[16–19] Our group concentrates on the synthesis of metal and metal oxide nanostructures with controlled shape and morphology.[20–26] In this paper, we describe the synthesis of a Zn-doped TiO_2 nanowall (ZnTNW) with a highly porous (001) face directly on the substrate surface *via* a liquid-phase deposition (LPD) method using a new fluoride scavenger, $ZnNO_3$, instead of the boric acid, normally used in the LPD process.[27–29] Field emission scanning electron microscopy (FESEM) and high resolution transmission electron microscopy (HRTEM) analysis revealed that the nanowall is constructed of a nanocuboid structure that is assembled so that it resembles a brick-like arrangement. This construction is extended to the surface of the nanowall and produces a surface with a high number of defects and porous structures. Such structural properties have caused the ZnTNW to exhibit excellent photocatalytic properties in the photodegradation of methylene blue (MB) with turnover number (ToN) and turnover frequency (ToF) values as high as 760 min^{-1} and 11 min^{-1}, respectively. This result is much higher compared to the results obtained with undoped TNW or other TiO_2 morphology, such as poriferous TiO_2 microtablets (PTMs), for multiple orders. The ZnTNW may find extensive use in solar cell applications and catalysis.

Experimental section

Materials and methods

ZnTNW growth on an indium tin oxide (ITO) substrate was prepared using a modified LPD method. In a typical procedure, the ZnTNW on the ITO surface were prepared by simply immersing a clean ITO substrate into a 20 mL solution that contains a mixture of aqueous solutions of 5 mL of 0.5 M ammonium hexafluorotitanate $[(NH_4)_2TiF_6]$ (Sigma-Aldrich, USA), and 1 mL of 0.5 M $Zn(NO_3)_2 \cdot xH_2O$ in the presence of 1 mL of 0.5 M hexamethylene tetramine (HMT) surfactant. In this study, the $Zn(NO_3)_2 \cdot xH_2O$ was used as the fluoride ion scavenger, replacing the boric acid that was used in conventional LPD methods for growing the TiO_2 films. Prior to the growth process, the solution was mixed ultrasonically for 2 minutes to obtain a well-mixed solution. The growth process was carried out in a temperature controlled water bath system with a growth time as long as 5 h. The effect of growth temperature was also studied by varying the water bath temperature from 50 to 90 °C.

After the growth process, the substrate was removed from the solution, rinsed with copious amounts of pure water and then dried with nitrogen gas. All the chemicals used in this research were purchased from Sigma-Aldrich Company, USA and used as received. The ITO was obtained from the Zhuhai Kaivo Optoelectronic Technology Co., Ltd, China with a sheet resistance of approximately 9–22 Ω per square.

The morphology and the crystallinity of the ZnTNWs were examined using FESEM (Hitachi S-4800) operating at 2 kV and HRTEM (Zeiss Libra HRTEM 200 FE) operating at 200 kV, respectively. The crystal structure and phase of the samples was characterized by an X-ray diffraction (XRD) technique (Bruker D8 Advance system) with CuKα irradiation ($\lambda = 1.541$ Å) at a scan rate of 10° min^{-1}. The surface chemistry of the sample was studied by X-ray photoelectron spectroscopy (XPS) using KRATOS XSAM HS with AlKα radiation. The optical properties of the sample was examined by diffuse reflectance spectroscopy method using PerkinElmer Lambda 950.

Photocatalytic characterization

The photocatalytic properties of the ZnTNWs were evaluated using the degradation of MB dye under the illumination of an ultraviolet (UV) light source. A UV lamp (365 nm) with a power of 5 W was used in this study. In a typical procedure, 5 mL of 40 ppm of MB was prepared and exposed to the light source. The distance between the light source and the MB solution container was fixed at 10 cm. A single slide of ITO (size 1.0 × 1.0 cm^2) containing approximately 0.4 mg of TiO_2 nanocatalyst (measured using a gravimetry method) was immersed into the MB solution. The degradation kinetics of MB under the illumination of the UV light source in the absence and the presence of ZnTNW catalyst were evaluated by determining the optical absorbance of MB, particularly at its main absorption band centering at 665 nm, every 10 min of the reaction. The optical absorption was obtained using UV-Vis-near-infrared spectrometer (Perkin-Elmer, Lambda 950) with a spectral resolution of 0.2 nm. To verify the role of shape as well as the effect of Zn doping on the photocatalytic properties, photodegradation of MB in the presence of a TiO_2 microtablet and pristine TiO_2 nanowalls were also investigated. In order to obtain the concentration change of the MB solution upon photocatalytic degradation, a calibration curve of absorbance *versus* MB concentration was also plotted (see Fig. S1, ESI†).

Results and discussion

Zn-doped TiO_2 nanowall characterization

Unlike the normal LPD method that produces a continuous thin film of a Ti-complex on the substrate surface, in this work, vertically oriented and branched nanowalls of Zn-doped TiO_2 were obtained. Fig. 1 shows a typical FESEM image of ZnTNWs grown on an ITO substrate prepared using a growth solution containing equimolar (0.5 M) $(NH_4)_2TiF_6$, Zn $(NO_3)_2 \cdot xH_2O$ and HMT at a temperature of 90 °C for 5 h. As Fig. 1 shows, the

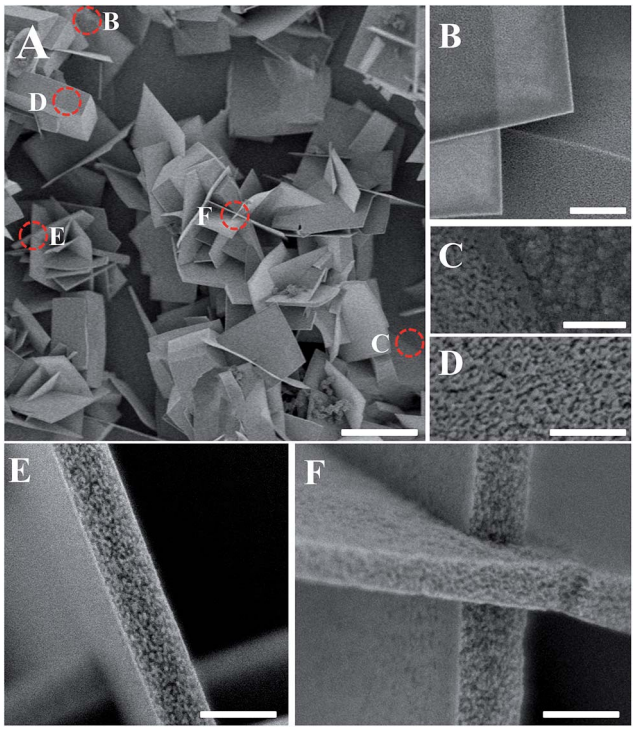

Fig. 1 (A) FESEM image of ZnTNW growth on the ITO surface prepared using an equimolar mixture (0.5 M) of $(NH_4)_2TiF_6$, $Zn(NO_3)_2 \cdot xH_2O$ and HMT. Growth temperature and growth time are 90 °C and 5 h, respectively. (C) and (D) show typical base and surface of the nanowall. (E) and (F) show the typical shape of the nanowall. Scale bars are 1 μm for (A), 500 nm for (B) and 100 nm for (C) to (F).

ZnTNWs are projected from the substrate surface (see Fig. 1C) and grow to a high density covering up to approximately 70% of the substrate surface. The individual nanowall construction of the ZnTNWs has a perfect square shaped morphology (see Fig. 1B) with a width and length that can be up to several micrometers and the thickness is in the range of 30 to 60 nm. Nevertheless, nanowalls with a thickness of several hundreds of nanometers were also obtained. However, its percentage was less than 5% of the product. Interestingly, the nanowall surface property is poriferous instead of a solid structure. High-resolution FESEM image as shown in Fig. 1D–F indicates that the surface is constructed by fibril structures (diameter and length are approximately 5 and 10 nm, respectively), which are likely to be projected from the bulk structure of the nanowall. Such a property probably makes the nanoplates electronically transparent at such a "high" thickness (50 nm) so that the stacked structure behind the nanoplate can be seen (see Fig. 1B). Even though the ZnTNWs are constructed by perfect square shaped nanowall branches, the orientation of the branches are irregular, and project from a parent nanowall. Nevertheless, the projected branches are mostly formed from the center position of the "parent". The high energy surface atom site at the center of the nanoplate can be the driving force for the re-nucleation and the branches projection. It is true that the projection of the nanowall branches from different positions on the parent surface was also obtained and their yield is also quite high. However, their formation seemed to be the result of a collision amongst the adjacent growing branches.

While the FESEM analysis reveals the surface structure properties of the nanowalls, the HRTEM analysis reveals its bulk structure and crystallinity. Fig. 2A shows a typical nanowall sample observed on the transmission electron microscopy (TEM) grid. The higher resolution image in Fig. 2B and C further confirms the structure that is constructed from smaller particles, arranged in a good order to form the nanowall geometry. The oriented-attachment process[30] is assumed to be the key factor that drives the formation of this structure, a phenomenon that is also observed in the formation of a PTM on the ITO substrate surface.[31] As observed in the FESEM image, the TEM analysis also indicates that the surface is not a solid (smooth) structure but contains large scale of voids or pores. Because most of the surface reaction and charge transfer is more active on the defects or high energy sites,[32] the TiO_2 with the present morphology promises enhanced performance in catalysis and solar cell applications. In contrast to the low resolution analysis, the high resolution image reveals that the nanowall is apparently single crystalline in nature because of the appearance of a continuous lattice fringe without the presence of twinning or dislocation (see Fig. 2D). This implies that the nanowall formation may involve a perfect oriented attachment process. According to the lattice fringe spacing value obtained, namely 0.19 nm, it can be understood that the nanoplates are characterized by the (100) plane, which is the second highest energy plane of anatase TiO_2.[33] The selected area electron diffraction (SAED) analysis further confirms the single crystallinity nature of the structure as well as the formation of the (001) face. Fig. 2E and F are the raw and the reconstructed SAED pattern from the nanowall surface. As can be seen from the raw pattern, the "square-shaped" SAED pattern, the characteristic of the (001) face, cannot be seen directly from the

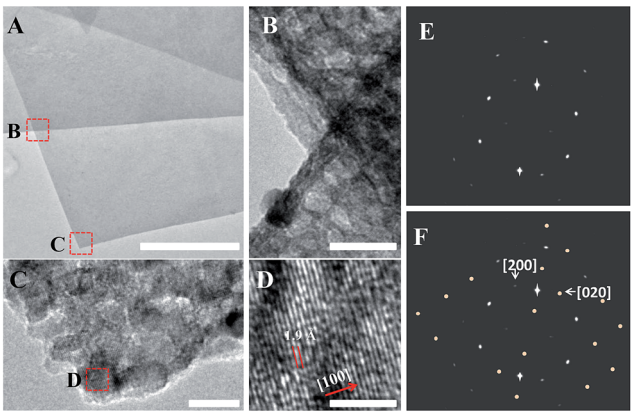

Fig. 2 Low (A–C) and high resolution (D) TEM images of a Zn doped TiO_2. The low resolution images show the stacking nanowall and the intersection of the stacked nanowall (B and C). The high resolution images (D) show the single crystalline nature of the nanowall with the orientation growth of [100]. (E) and (F) are the original and reconstructed SAED patterns, respectively. Scale bars are 1 μm, 20 nm, 5 nm, 2.5 nm for (A), (B), (C) and (D), respectively.

figure because of the absence of some lattice fringes. However, the reconstructed pattern shows the formation of a square shaped SAED pattern, and thus confirms the (001) face of the nanowall. Judging from the FESEM image in Fig. 1 and the low resolution TEM image in Fig. 2B–D, the absence of some lattice fringes can be understood to be simply because of the nature of the surface that contains a high number of void structures and porous properties at which the electron beam is weakly diffracted or un-diffracted.

As has been mentioned in the experimental section as the present structure was prepared in a growth solution that is also composed of the Zn^{+} precursor ($ZnNO_3 \cdot H_2O$), the presence of Zn^{+} in the nanocrystal is expected as this experiment was an attempt to dope the TiO_2 with this element. However, the HRTEM analysis shows no indication of a Zn or ZnO phase present in the nanocrystals. An XRD analysis was then carried out on the sample to verify the phase and the crystallinity of the TiO_2 as well as of the Zn presence in the nanocrystal. The results are shown in Fig. 3. To our surprise, except for the presence of the anatase phase of TiO_2 (JCPDS no. 21-1272 standard pattern of anatase TiO_2), the X-ray spectrum did not show the presence of either Zn or ZnO phases in the nanocrystal, which implies

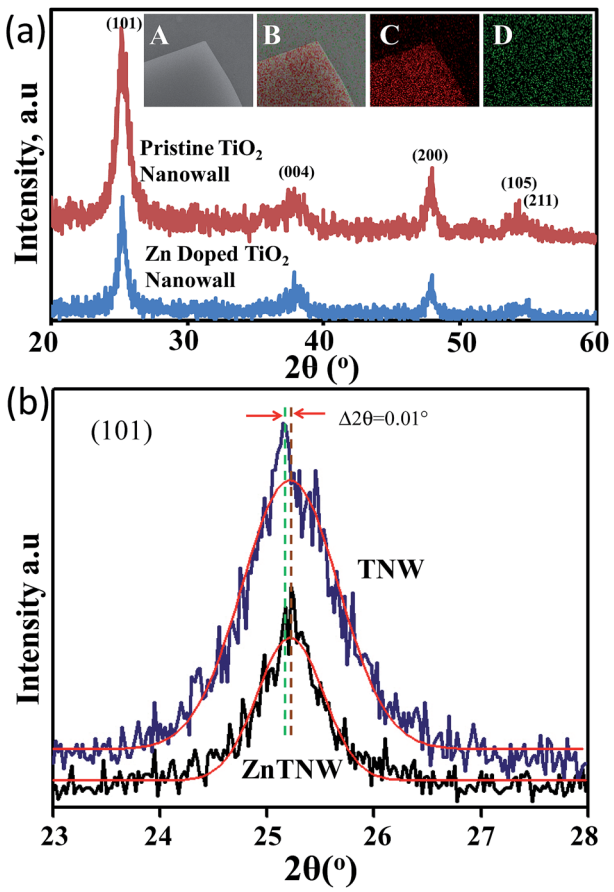

Fig. 3 (a) XRD spectra of pristine TNW and ZnTNW. Inset shows pictographs of the unmapped surface of ZnTNW (A) and Ti and Zn mapping (B), Ti (C) and Zn (D) element mappings. The Ti element is indicated by red colour, while the Zn element was green. (b) High-resolution spectra of (101) peaks with curve fitting.

that an effective substitution of Zn^{+} into the anatase TiO_2 nanocrystals has occurred. Such a process seems valid as the presence of the (101) peak position shifts to the right from the pristine anatase TiO_2 (see Fig. 3b). A detailed curve fitting analysis of the XRD spectra indicates the peak shifting is as high as 0.01°. Such shifting reveals that there is a reduction in the interplanar distance of the crystal lattice upon Zn atom substitution.[34] This is proven by a higher crystallite size of ZnTNW compared to pristine TNW (see Table S1, ESI†). Increasing the crystallite size reflects the reduction of the lattice spacing. Unfortunately, although the HRTEM result in Fig. 2 suggested that the crystal growth preference is towards [001], the XRD spectra show unclear crystal growth preference. It is true that the (004) peak should be higher or comparable to the (101) peak for preferential growth towards this direction. However, this could be because of the nature of the TNW surface that is porous, exposing a stable (101) lattice plane at the body of nanofiber. Thus, the X-ray diffraction from (101) lattice plane still very high. A detailed list of crystallinity parameters of TNW and ZnTNW is presented in Table S1 (ESI†). Furthermore, X-ray energy dispersive analysis (EDX) was carried out on the sample. The results are shown in inset of Fig. 3. As was expected, the EDX elemental analysis successfully shows the presence of elemental Zn as well as Ti in the nanowall (see Fig. 3, inset (B)). The elemental mapping of the Zn and Ti in the nanowall indicated a homogeneous dispersion of Zn (shown by green dots) throughout the nanowall, confirming that there had been an efficient substitution of Zn into the TiO_2 lattice. Insets (C) and (D), also show that efficient substitution of Zn not only occurs in the nanowall but also in the TiO_2 nanostructures grown on the surface of the ITO substrate. One point to be noted here, the O elemental mapping was too strong because of the contribution of the O element of the substrate. Therefore, its distribution in the nanoplate could not be determined.

The presence of Zn doping in the nanostructure, which is probably substituted into the TiO_2 crystallite, was confirmed by EDX analysis, and the use of XPS analysis provides further verification of such a process. Fig. S2† shows the wide scan XPS analysis without carbon correction indicating the presence of Ti, Zn, and O elements. The fitted spectrum for Ti 2p is shown in Fig. 4A with the presence of two peaks namely Ti $2p_{3/2}$ and Ti $2p_{1/2}$. Both of these peaks can be observed at 458.63 eV and 464.2 eV, but are, however, much lower in binding energy compared to results of other reported research work[35] even though they still falls in to the Ti $2p_{3/2}$ and Ti $2p_{1/2}$ oxidation state group region. The shifting towards a lower binding energy indicates that the TiO_2 nanoplate investigated does indeed have a high oxygen vacancy which might have been contributed by the presence of the Zn element in the samples. The Ti $2p_{3/2}$ orbital, is composed of two Gaussian–Lorentzian (GL) mixed functions at 459.8 and 458.63 eV, which correspond to the Ti^{4+} and Ti^{3+} states, respectively. Judging from the intensity of the GL function in the $2p_{3/2}$ orbital, the surface chemistry of the ZnTNW nanowall is characterized by a dominant Ti^{3+} state. A similar phenomenon was also observed for pristine TNW. The present result is unusual for the TiO_2 nanostructure, which is normally dominated by Ti^{4+} state for a (101) lattice-plane

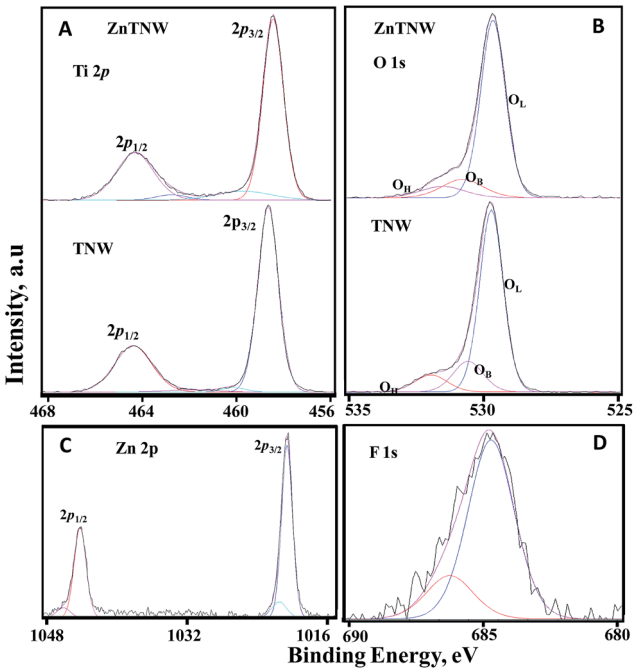

Fig. 4 XPS spectrum of Zn doped TiO_2 nanoparticles and pristine TNW for (A) Ti 2p, (B) for O 1s, and (C) Zn 2p. (D) is spectrum for F 1s, proving that the surface was fluorinated.

dominated surface. This is an indication that the surface of the nanowall contains highly reactive five-fold coordinated Ti with a strained Ti–O–Ti bond. Novel properties were expected to be generated from this nanostructure. Fig. 4B shows the fitted spectrum for the oxygen core level, O 1s of a Zn doped TiO_2 nanoplate. From the spectrum, is seen that there exists three asymmetric patterns for O 1s namely O_L, O_B and O_H. It is well known that the pattern O_L and O_B at 529.25 and 531.3 eV was attributed to the lattice oxygen and bridging oxygen of TiO_2. While the O_H band obtained in the spectrum at 532.1 eV was because of the chemisorbed water on the TiO_2 surface, which leads to the formation of Ti–O–O and Ti–OH. For the OH peak, its intensity is much lower compared to the O_L and O_B. This is an indication of a high purity property. The appearance of these asymmetric patterns are normal and in agreement with the reported result. In addition, the peaks in the spectrum actually appear to be shifted to the lower energy compared to the pristine TiO_2. This is attributed to the effect of the Zn doping in the TiO_2 nanocrystals.[36]

Together with the Ti, Zn and O spectra, the F 1s spectrum is also observed in the XPS results (see Fig. 4D). However, it was assumed that the presence of fluorine in the nanostructure is not related to lattice impurity but is related to the surface adsorption instead.[37] As has been mentioned earlier in the experimental section, abundant fluorine ions may be produced during the reaction and they are freely available in the bulk solution because no fluoride scavenger was used in this study. They may then absorb onto the surface of the nanocrystal and might also have played a particular role in controlling the shape of the nanocrystal. As can be seen from Fig. 4D, the F 1s intensity in the Zn-doped TiO_2 is much lower than the pristine TiO_2. This could be as the result of the effective scavenging process by the Zn ions.

The exact mechanism of the formation of vertical platelet structure is not yet clearly understood. Nevertheless, the crystal plane passivation, of the (001) plane in this case as confirmed by the XRD analysis, *via* fluorination and HMT adhesion is assumed to be the driving factor for the formation of such morphology.[38–41] It is well known that the hydrolysis of $(NH_4)_2TiF_6$ by the water may produce fluorine anions in the reaction. They may then easily attach onto, and passivate, the high energy plane of the TiO_2 crystal (001), directing the crystal growth towards the [100] direction. XPS analysis results as shown in Fig. 4 verify that such a fluorination process occurs. Thus, a platelet structure can be formed. However, despite the fact that such a phenomenon has also been observed in the recently reported result, for example in the formation of TiO_2 nanocube and microtablets, their effect in the formation of platelet structure in this case is not so crucial but seems to be complementary to the significant role of HMT. In our trial, we found that no vertical nanoplate was grown on the ITO surface when no HMT was present in the reaction. To prepare high-density ZnTNWs, the concentration of HMT should be at least 0.4 M. At a lower concentration or in an extreme case in the absence of HMT, TiO_2 films composed of a quasi-spherical morphology were produced. The sample shown in Fig. 1 was prepared using HMT with concentration of 0.5 M. If the HMT concentration increases further from this value, high-density ZnTNWs with larger thickness and intense branching as well as platelet overlapping were formed. The results are shown in Fig. S3 (ESI†). Such an insignificant role of the surface fluorination effect in the formation of the nanowall is indicated by the successful growth of ZNTNW even though the limited availability of surface fluorination (indicated by the low intensity of F 1s peaks in the XPS spectrum) because of the use of Zn ions as fluoride scavengers. In addition, to prepare the nanowall, the growth temperature should be around 90 °C, lower temperatures, such as 50 °C and 70 °C, only produce smaller sized and low yield nanowalls (see Fig. S4(A) and (C) in the ESI†). If the temperature is further lowered, for example at room temperature, neither nanowalls or other nanostructures were formed. Meanwhile, the nanocrystal growth at temperatures higher than 90 °C was not obtained because of the boiling of the aqueous reaction media.

Considering the reaction times for nanowall growth, the nanowalls were found to formed as early as 3 h but the high density nanowall growth was not obtained until 4 h into the process (see Fig. S5(A) and (C) in the ESI†). The growth density increases with the increasing of the growth time.

The oriented attachment is considered as the main mechanism for the formation of nanowalls on the substrate.[42] From the FESEM analysis of the "bulk-volume" structure of the nanowall (see Fig. 5), it was hypothesized that at the beginning of the reaction, nanocuboid structures were formed both in solution and on the surface. Because they contained a high energy facet, they were attached both onto available nanocuboids on the surface and also formed in the solution to

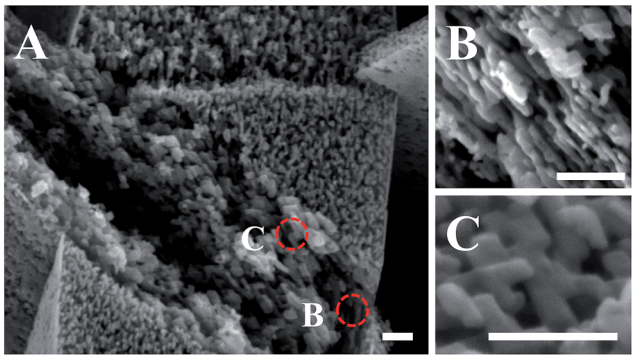

Fig. 5 (A and B) FESEM image of the "bulk-volume" structure of the nanowall showing nanocuboid stacking. (C) High-resolution FESEM image showing the detailed structure of a nanocuboid. Scale bars are 100 nm.

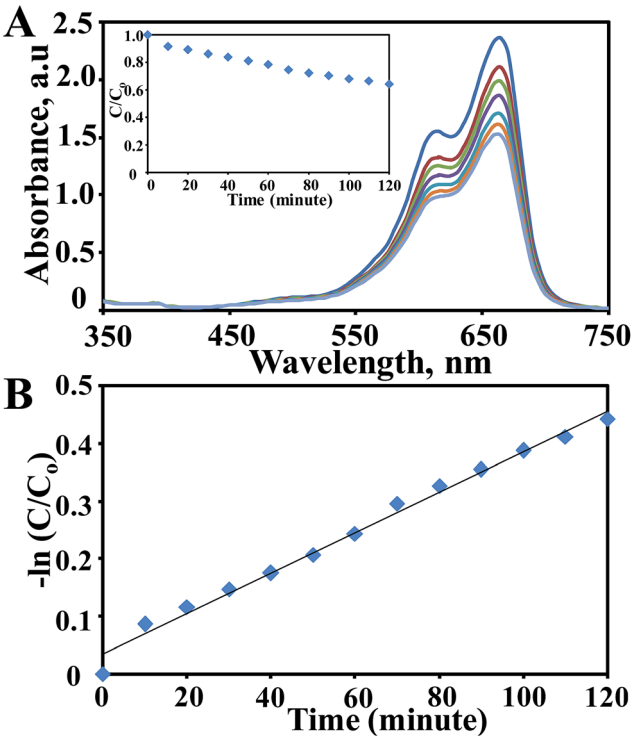

Fig. 6 Typical absorbance (A) and reaction kinetic rate (B) for MB degradation under UV irradiation in the presence of the ZTNW nanocatalyst. Inset in (A) shows the percentage degradation of MB during the reaction.

minimize the surface energy. At the particular stage at which the reaction of the chemical potential decreases because of the consumption of precursors, the nanocuboid shape and size are changed to a "nanowire" like structure instead of the nanocuboid. Thus, this new structure constructs the surface of the nanowall, forming a highly porous nanowall surface. For the branched nanowall formation, it is considered to be because of the re-nucleation of the nanocuboid onto the higher energy site of the nanowall, namely at the centre position of the nanowall. Considering the size of the nanowall branches, its formation is predicted to occur at the earlier stage of the growth process. It is true that the nanowall branches are also observed at a non-central position of the main nanowall. However, their formation is because of the collision of adjacent growing nanowalls.

Heterogeneous photocatalytic characterization

A heterogeneous catalytic property of ZnTW was investigated using photodegradation of MB under a UV lamp at a wavelength of 365 nm. Fig. 6A shows the typical dynamic absorption spectra of MB during the photocatalytic degradation under UV light exposure. As Fig. 6A reveals, the concentration of MB effectively decreases with the increasing time during the photocatalytic degradation reaction that is indicated by the decrease in the absorption intensity at 665 nm. Inset in Fig. 6A shows the corresponding degradation kinetics of MB in the presence of ZnTNW obtained by plotting the absorbance value at the peak position over the reaction time.

As can be seen from Fig. 6, the MB significantly decreases during the reaction process and is reduced to approximately 36% over the course of the reaction, *i.e.*, 120 min. By considering the initial MB concentration of 40 mg L^{-1}, the final concentration is equivalent to 25.8 mg L^{-1}. By taking into account the specific surface area (S_{BET}) of the ZnTNW nanocatalyst obtained from the Brunauer, Emmett and Teller (BET) analysis of as high as 0.050 m^2 and the dynamic cross-section of MB molecules is as high as 197.2 $Å^2$, these result are equivalent to a ToN and a ToF as high as 760 min^{-1} and 11 min^{-1}, respectively. Although, the ToN and ToF values of the system are marginal compared to recently reported results, however, in terms of the heterogeneous photocatalytic reaction in which the molecules' adsorption onto the catalyst surface becomes a crucial issue because of the presence of the substrate surface effect as well as the solid–liquid interface barrier that may give a repulsion force to the approaching molecules, this result is considerably high. In addition, because not all of the available surface area is available for the attachment of MB molecules, for example the lower level surface, the ToN and ToF should be much higher compared to these values.

By considering the amount of ZnTNW nanocatalyst available on a single slide substrate, approximately 0.4 mg, the present result is 100 times higher compared to the reported results using an homogeneous catalytic reaction. This could be directly related to the following reasons: firstly, as judged from the XRD and HRTEM results, the present nanostructure is the structure with the highest available (001) surface plane for anatase TiO_2 that would facilitate effective adsorption and degradation of MB molecules. Analysis of the catalytic activity of ZnTNW in the dark (see curve b in Fig. S6, ESI†) showed that the ZnTNW has readily catalyzed the degradation reaction of MB. It is indicated by a significantly high MB degradation (approximately 6%) for the immersion time of 120 min. It is already well known that the (001) plane of anatase TiO_2 also readily splits the water molecules without an externally applied field. Secondly, the ZnTNW possesses a high surface area for surface reaction. BET analysis revealed that the specific surface area of ZnTNW on a single ITO slide is as high as 0.050 m^2 or an equivalent of 114.69 g m^{-2} (see ESI† for detailed BET analysis). Despite this, not all the area may

be involved in the surface reaction, the high energy property of the (001) plane of anatase TiO_2 may facilitate highly efficient heterogeneous catalytic degradation of MB. To further verify the unique effect of such a high energy plane, the photodegradation rate analysis was carried out. The result is shown in Fig. 6B. Based on this result, it is found that the reaction follows a first-order kinetic reaction with a rate as high as 0.0035 min^{-1}, in which the catalytic efficiency solely depends only on the surface reactivity of the nanocatalyst. This reflects that, as the surface of the nanocatalyst covered by the MB molecules decreases with time because of MB degradation, the formation of a OH^- radical ion is enhanced as the result of a facile acceptance of photoexcited electrons by the water molecules,[43] thus, linearly accelerating the degradation process.

These effects were further examined by varying the catalyst concentration in the reaction by simply introducing up to four ITO slides containing the ZnTNW nanocatalyst. The results are shown in Fig. 7. As can be seen, the degradation rate linearly increases when the number of ITO slides containing the ZnTNW nanocatalyst are increased in the reaction. For example, the reaction rate is almost double (from 36% to 62%) when two slides containing nanocatalyst are used in the reaction. However, the reaction rate only increases to approximately 70% and 80% when the number of slides increases to three and four, respectively. Although there are "non-linear" increases in the degradation rate when the amount of catalyst increases in the reaction, it was thought that the reaction still obeys first-order reaction kinetics. These results could simply be related to the design of the container for the MB solutions that makes the placement of the slides as well as the placement for the UV light source not optimized. Thus, a linear increase in the degradation rate as the amount of nanocatalyst increases was not achieved.

The effect of light source irradiation on the degradation of MB can be neglected here because of the low power UV light source was used in this study (5 W). Analysis of the effect of light irradiation on the MB degradation further verified this analysis (see curve A, Fig. S6, ESI†).

So far, the ZnTNW has been shown to have a highly efficient catalytic effect on the photodegradation of MB. To obtain the effect of Zn doping on the nanostructure, the catalytic properties of pristine TNWs on the degradation of MB were also examined. The result is shown in Fig. 8A (curve a). As Fig. 8A reveals, the TNW exhibits highly efficient catalytic properties in the degradation of MB. It was found that, for a reaction time of 120 min, the concentration of MB changed from 40 mg L^{-1} to 27.35 mg L^{-1}, which is equivalent to a decrease as high as 31.6%. Kinetic analysis found that the degradation rate was as high as 0.0029 min^{-1} in the TNW system. A decrease as high as 35.9% or a degradation rate of 0.0035 min^{-1} was found for ZnTNW in comparison. It is true that this result shows only relatively small improvement of ZnTNW compared to the pristine TNW. The high efficiency of TNW can be understood to be the result of the fact that TNW possesses a large area of (001) high energy facet, so that efficient catalytic photodegradation can be readily achieved on the pristine TNW. Nevertheless, it is an indication of the improved performance of TNW when doped with the Zn.

In order to further verify the specialty of the present structure of anatase TiO_2, the catalytic performance with different structures of TiO_2 was compared with PTM (see Fig. S7, ESI†), which is also characterized by a high energy plane of (001).[31] The result for the kinetic degradation analysis is shown in Fig. 8A (curve c). As can be seen from the figure, it is true that the degradation kinetic rate for PTM is relatively higher than that of ZnTNW by about 10%. However, one point to be noted here, because the specific surface area of PTM used here is 0.1227 m^2, which is double of the ZnTNW, its ToN is inferior to that of the ZnTNW system. The results are shown in Fig. 8B. The detailed properties and the catalytic performance of ZnTNW, TNW and PTM

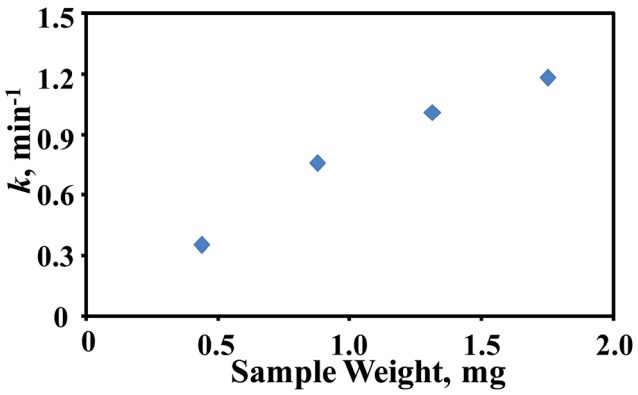

Fig. 7 Kinetic rate of MB degradation (k) for different weights of nanocatalyst.

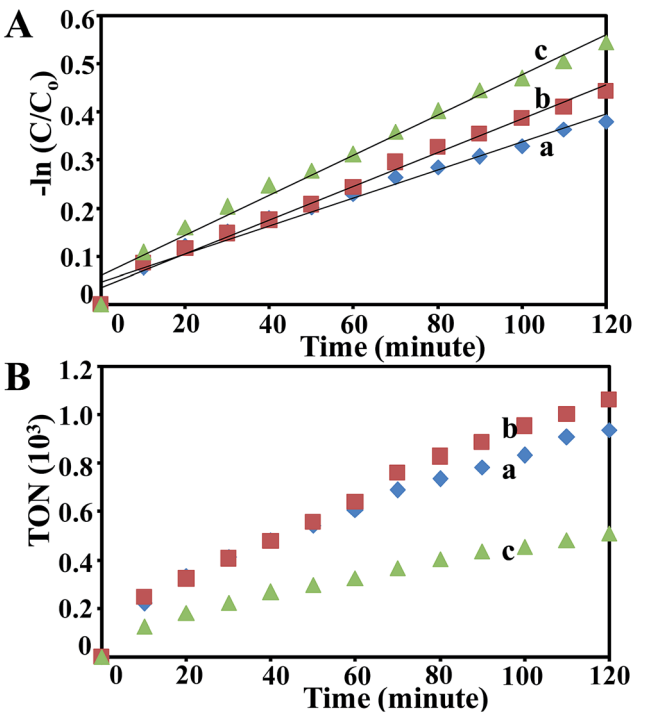

Fig. 8 (A) Kinetic rate of MB degradation under UV irradiation in the presence of different nanocatalyst morphologies, TNW (a), ZTNW (b) and PTM (c). (B) shows the corresponding ToN analysis results.

are summarized in Table 1. On the basis of these results it can be mentioned that the ZnTNW exhibit a peculiar catalytic property because they possess a large scale, high energy facet and Zn doping.

While the present nanostructure has been proven to be superior over other morphologies, the role of Zn doping in the photocatalytic performance was also examined. ZnTNWs with three different Zn contents were prepared by introducing a zinc salt with a concentration of 0.2, 0.5 and 1.0 mM into the standard growth solution. From this reaction, ZnTNWs with Zn contents as high as 4.77%, 7.65% and 2.32%, respectively, were produced. In a typical procedure, it was found that the photocatalytic performance increases with the increase in the Zn doping concentration. For example, the photodegradation kinetic rate was enhanced from 0.0021 min^{-1} to 0.0035 min^{-1} if the concentration of Zn ion content (from the EDX analysis) was elevated from 2.32% to 7.65%. The results are shown in Fig. S8 (ESI†). Although, the improvement is not linearly correlated to the Zn content, this result more or less provides clear evidence of the role of Zn doping in the improvement of the photocatalytic performance of the ZnTNW. It is believed that the performance can be further optimized if the Zn content can be further be modified. The synthesis of ZnTNW with higher concentrations was attempted by increasing the zinc salt concentration in the reaction. Unfortunately, further increases in the zinc salt concentration produced ZnTNW nanocrystals with a lower Zn content. For example, the Zn content in the sample prepared using a 1.0 mM zinc salt is lower than the one prepared using 0.5 mM. It was also found that the structural stability of the ZnTNW decreased with the increasing of zinc salt concentration in the reaction, which was the result of distortion of the growth kinetics in the reaction upon the presence of a higher concentration of the zinc salt. Nevertheless, the attempt to find the optimum condition is in progress.

To further elucidate the effectiveness of the structure and Zn-doping effects on the photocatalytic properties, the extent of the effect of the light absorption on photocatalytic performance by the ZnTNW was evaluated using diffuse reflectance spectroscopy. The result is shown in Fig. S9 (ESI†). In a typical process, it was found that both samples (pristine and Zn-doped TNW) exhibit, surprisingly, a relatively lower reflectance which is independent of the wavelength – compared with the standard Degussa P25 sample.[44] In the UV region, for example, which is associated with the excitonic character, the reflectance is as low as 6%. It was thought that this could be related to the strong absorption of UV light by the ITO-glass substrate instead of the ZnTNW because of the transparent and porous nature of the nanowall sample. Meanwhile, in the visible region (400 to 800 nm), lower reflectance can be associated with the porous nature of the TNW surface, which may behave as light cavities at this wavelength region. The enhancement of defect related absorption could also be responsible for the increase of the light absorption in this region. Thus, the effect of light absorption enhancement on the improvement of the photocatalytic activity can simply be neglected. Nevertheless, the ZnTNW exhibits slightly lower reflectance than the pristine TNW. This is strong evidence for the enhanced electronic excitation in the nanostructure upon doping. It is well-known that during the photo-irradiation of TiO_2, the electrons are excited to the conduction band (CB) of TiO_2 while leaving the hole at the valence band (VB). The hole in the VB then reacts with water molecules producing hydroxyl radicals. Meanwhile, the electron in the CB will reduce the formed oxygen in water, forming oxide anion radicals. The oxide anion radical will then react with water and again produces the hydroxyl radical ($OH^{\bullet}$). Finally, the $OH^{\bullet}$ radical will react with MB, resulting in the degradation of the MB.

During the MB degradation process, the adsorption of O_2 by TiO_2 was necessary to produce the superoxide ($O_2^{\bullet}$) radicals as these radicals will then help in producing other more reactive radical from the hydroxyl groups that exist in the solution. The $OH^{\bullet}$ radical played a crucial part in the degradation of MB because of its lower energy of 2.8 eV. It has been well-known that the surface reactivity of the (001) plane was much higher than the typical (101) plane of TiO_2, with a surface energy of 1.44 J m^{-2}. Higher surface reactivity contributes to much higher $O_2^{\bullet}$ adsorption on the surface of TiO_2.

The improvement of the photocatalytic properties of the TNW upon Zn doping can be understood from the point of view of: (i) enhancement of surface activity because of the increase of surface oxygen vacancy density and impurity energy level.[15] XPS analysis as shown in Fig. 4B validates such a process as the energy state of O 1s decreases by several orders of magnitude, which is the key parameter for hydroxyl radical formation, upon doping with Zn. This will further enhance the surface energy for several orders higher, producing more reactive surface to facilitate active $O_2^{\bullet}$ adsorption on the surface. (ii) Increasing of the Fermi level energy and the reduction of the conduction band minimum when the TNW is doped with the Zn.[45] This in turn lowers the energy required to photoexcite the electron from the VB. Diffuse reflectance spectra as shown in Fig. S9† confirms such an energy gap lowering, which is show as an increase of the UV light reflected by the ZnTNW. Improvement of the hydroxyl radical formation is expected from this process. Thus, higher photoreactivities are expected to occur on the ZnTNW compared to the pristine TNW or PTM.

Considering the morphology of the ZnTNW composed of a fibrous surface structure with a (001) high energy lattice plane,

Table 1 Nanocatalyst properties and photocatalytic parameters

Sample	S_{BET} (m^2 g^{-1})	Catalyst weight (mg)	Reaction rate, k (min^{-1})	ToN	ToF (min^{-1})
TNW	114.8	0.4	0.0029	689.1	9.84
ZTNW	114.9	0.4	0.0035	759.52	10.85
PTM	160.9	0.7	0.00418	367.97	5.26

the nanostructure may be exposed to a structural deformation as the cost of photocatalytic activity. FESEM analysis was carried out after the use of the sample to confirm its chemical stability. The result is shown in Fig. S10.† Interestingly, despite a high energy plane with fibrous morphology, the sample shows no sign of structural damage or annealing, confirming the nanostructure feature has excellent chemical stability. Thus, it should find a potential use in photocatalysis, sensor or solar cell applications.

The present photocatalytic performance was evaluated by considering the specific surface area obtained from BET analysis (see nitrogen adsorption characteristic in the ESI†) and its surface chemical state is interpreted *via* XPS. It is true that the active site for catalytic reaction on the surface of catalyst should be examined *via* temperature programmed desorption or temperature programmed reduction. However, because of the unavailability of the apparatus, the active site was approximated using the BET surface area analysis result. This is assumed to be applicable because the BET is solely based on the analysis of nitrogen gas adsorption and desorption on the TiO_2 nanostructure. Nevertheless, the active site is predicted to be less than the BET surface area because the adsorption of the MB molecules during the photodegradation should be on the most accessible site only, instead of on the available surface area. Therefore, the value of the ToN and ToF should be much higher compared to the ones presented earlier. The active catalytic site of the TNW is being examined and the results will be reported separately.

Conclusions

A Zn-doped anatase TiO_2 nanowall with a (001) facet and porous structure was synthesized directly on the ITO substrate surface. The novel structure is constructed of nanocuboid structures that are arranged in a brick-like assembly, producing highly porous properties. The (001) high energy plane nanowall formation is assumed to be because of the combinative effect of HMT and the surface fluorination process during the growth process. Owing to its unique morphology with the high energy (001) facet and efficient Zn metal doping, the ZnTNW exhibited superior heterogeneous catalytic properties compared to other structures with rich (001) faces, such as PTM, as well as pristine TNW with ToN and ToF in the photocatalytic degradation of MB as high as approximately 760 min^{-1} and 11 min^{-1}, respectively. The ZnTNW may find potential uses in heterogeneous catalytic, sensor and solar cell applications.

Acknowledgements

The authors would like to acknowledge Universiti Kebangsaan Malaysia and Ministry of Higher Education (MOHE), Malaysia for funding this work under research grants HiCOE Project and FRGS/1/2013/SG02/UKM/02/8. The authors also are grateful for the financial support received from Ministry of Science, Technology and Innovation (MOSTI), Malaysia for the funding under Science Fund grant (06-01-02-SF1157).

Notes and references

1 W.-J. Ong, L.-L. Tan, S.-P. Chai, S.-T. Yong and A. R. Mohamed, *Nanoscale*, 2014, **6**, 1946–2008.
2 E. J. W. Crossland, N. Noel, V. Sivaram, T. Leijtens, J. A. Alexander-Webber and H. J. Snaith, *Nature*, 2013, **495**, 215–219.
3 X. Zhao, W. Jin, J. Cai, J. Ye, Z. Li, Y. Ma, J. Xie and L. Qi, *Adv. Funct. Mater.*, 2011, **21**, 3554–3563.
4 S. M. Roopan, F. N. Khan, J. S. Jin and R. S. Kumar, *Res. Chem. Intermed.*, 2011, **37**, 919–927.
5 H. G. Yang, C. H. Sun, S. Z. Qiao, J. Zou, G. Liu, S. C. Smith, H. M. Cheng and G. Q. Lu, *Nature*, 2008, **453**, 638–641.
6 J. Yu, J. Fan and K. Lv, *Nanoscale*, 2010, **2**, 2144–2149.
7 G. Liu, C. Y. Jimmy, G. Q. M. Lu and H.-M. Cheng, *Chem. Commun.*, 2011, **47**, 6763–6783.
8 W. Yang, J. Li, Y. Wang, F. Zhu, W. Shi, F. Wan and D. Xu, *Chem. Commun.*, 2011, **47**, 1809–1811.
9 Y. Luan, L. Jing, Y. Xie, X. Sun, Y. Feng and H. Fu, *ACS Catal.*, 2013, **3**, 1378–1385.
10 Y. Wang, H. Zhang, Y. Han, P. Liu, X. Yao and H. Zhao, *Chem. Commun.*, 2011, **47**, 2829–2831.
11 B. Liu and E. S. Aydil, *Chem. Commun.*, 2011, **47**, 9507–9509.
12 S. Wang, H. Qian, Y. Hu, W. Dai, Y. Zhong, J. Chen and X. Hu, *Dalton Trans.*, 2013, **42**, 1122–1128.
13 L. Yang, Y. Zhang, W. Ruan, B. Zhao, W. Xu and J. R. Lombardi, *J. Raman Spectrosc.*, 2010, **41**, 721–726.
14 G. Zhu, Z. Cheng, T. Lv, L. Pan, Q. Zhao and Z. Sun, *Nanoscale*, 2010, **2**, 1229–1232.
15 K.-P. Wang and H. Teng, *Phys. Chem. Chem. Phys.*, 2009, **11**, 9489–9496.
16 F. Huang, Q. Li, G. J. Thorogood, Y.-B. Cheng and R. A. Caruso, *J. Mater. Chem.*, 2012, **22**, 17128–17132.
17 Z. Ali, S. N. Cha, J. I. Sohn, I. Shakir, C. Yan, J. M. Kim and D. J. Kang, *J. Mater. Chem.*, 2012, **22**, 17625–17629.
18 K. Assaker, C. Carteret, T. Roques-Carmes, J. Ghanbaja, M.-J. Stebe and J.-L. Blin, *New J. Chem.*, 2014, **38**, 2081–2089.
19 M. E. Fragala, I. Cacciotti, Y. Aleeva, R. Lo Nigro, A. Bianco, G. Malandrino, C. Spinella, G. Pezzotti and G. Gusmano, *CrystEngComm*, 2010, **12**, 3858–3865.
20 A. Balouch, A. A. Umar, S. T. Tan, S. Nafisah, S. K. Md Saad, M. M. Salleh and M. Oyama, *RSC Adv.*, 2013, **3**, 19789–19792.
21 A. Balouch, A. Ali Umar, A. A. Shah, M. Mat Salleh and M. Oyama, *ACS Appl. Mater. Interfaces*, 2013, **5**, 9843–9849.
22 A. Ali Umar and M. Oyama, *Cryst. Growth Des.*, 2006, **6**, 818–821.
23 A. Ali Umar, M. Oyama, M. Mat Salleh and B. Yeop Majlis, *Cryst. Growth Des.*, 2010, **10**, 3694–3698.
24 S. T. Tan, A. A. Umar, A. Balouch, M. Yahaya, C. C. Yap, M. M. Salleh and M. Oyama, *Ultrason. Sonochem.*, 2014, **21**, 754–760.
25 A. A. Umar and M. Oyama, *Cryst. Growth Des.*, 2008, **8**, 1808–1811.
26 A. A. Umar and M. Oyama, *Cryst. Growth Des.*, 2007, **7**, 2404–2409.

27 S. Deki, H. Y. Y. Ko, T. Fujita, K. Akamatsu, M. Mizuhata and A. Kajinami, *Eur. Phys. J. D*, 2001, **16**, 325–328.
28 A. A. Umar, M. Y. A. Rahman, S. K. M. Saad, M. M. Salleh and M. Oyama, *Appl. Surf. Sci.*, 2013, **270**, 109–114.
29 W. Shao, F. Gu, L. Gai and C. Li, *Chem. Commun.*, 2011, **47**, 5046–5048.
30 D. Li, M. H. Nielsen, J. R. I. Lee, C. Frandsen, J. F. Banfield and J. J. De Yoreo, *Science*, 2012, **336**, 1014–1018.
31 A. Ali Umar, S. Nafisah, S. K. Md Saad, S. Tee Tan, A. Balouch, M. Mat Salleh and M. Oyama, *Sol. Energy Mater. Sol. Cells*, 2014, **122**, 174–182.
32 A. L. Linsebigler, G. Lu and J. T. Yates, *Chem. Rev.*, 1995, **95**, 735–758.
33 R. S. Kumar, M. Balasubramanian, M. Jacobsen, A. Bommannavar, M. Kanatzidis, S. Yoneda and A. L. Cornelius, *J. Electron. Mater.*, 2010, **39**, 1828–1831.
34 W. Wei, N. Yaru, L. Chunhua and X. Zhongzi, *RSC Adv.*, 2012, **2**, 8286–8288.
35 H. G. S. Yang, C. Hua, Q. S. Zhang, Z. Jin, L. Gang, S. S. Campbell, C. H. Ming and L. G. Qing, *Nature*, 2008, 453.
36 Y. Zhao, C. Li, X. Liu, F. Gu, H. Du and L. Shi, *Appl. Catal., B*, 2008, **79**, 208–215.
37 H. Zhang, P. Liu, F. Li, H. Liu, Y. Wang, S. Zhang, M. Guo, H. Cheng and H. Zhao, *Chem.–Eur. J.*, 2011, **17**, 5949–5957.
38 X. Han, Q. Kuang, M. Jin, Z. Xie and L. Zheng, *J. Am. Chem. Soc.*, 2009, **131**, 3152–3153.
39 J. Zhu, S. Wang, Z. Bian, S. Xie, C. Cai, J. Wang, H. Yang and H. Li, *CrystEngComm*, 2010, **12**, 2219–2224.
40 J. S. Chen, Y. L. Tan, C. M. Li, Y. L. Cheah, D. Luan, S. Madhavi, F. Y. C. Boey, L. A. Archer and X. W. Lou, *J. Am. Chem. Soc.*, 2010, **132**, 6124–6130.
41 H. Zhang, Y. Wang, P. Liu, Y. Han, X. Yao, J. Zou, H. Cheng and H. Zhao, *ACS Appl. Mater. Interfaces*, 2011, **3**, 2472–2478.
42 W. Q. Fang, J. Z. Zhou, J. Liu, Z. G. Chen, C. Yang, C. H. Sun, G. R. Qian, J. Zou, S. Z. Qiao and H. G. Yang, *Chem.–Eur. J.*, 2011, **17**, 1423–1427.
43 L. D. Sanchez, S. F. M. Taxt-Lamolle, E. O. Hole, A. Krivokapic, E. Sagstuen and H. J. Haugen, *Appl. Catal., B*, 2013, **142**, 662–667.
44 C. Feng, Y. Wang, Z. Jin, J. Zhang, S. Zhang, Z. Wu and Z. Zhang, *New J. Chem.*, 2008, **32**, 1038–1047.
45 Q. Meng, T. Wang, E. Liu, X. Ma, Q. Ge and J. Gong, *Phys. Chem. Chem. Phys.*, 2013, **15**, 9549–9561.